Research Article

Vu Thi Hau, Pham Hoai Linh, Pham Thu Ha, Nguyen Thuy Chinh, Ngo Thi Mai Viet, Dang Duc Dung, Nguyen Quoc Dung*, Thi Kim Ngan Tran*

Characterization and application of $Fe_{1-x}Co_xFe_2O_4$ nanoparticles in Direct Red 79 adsorption

https://doi.org/10.1515/chem-2024-0102
received May 27, 2024; accepted September 27, 2024

Abstract: Water pollution remains a significant global challenge, with dye contamination from industrial activities being particularly problematic. Adsorption is widely recognized as an efficient, rapid, and cost-effective method for pollutant removal. To enhance adsorption efficiency, researchers have increasingly focused on the development of reusable adsorbent materials. Magnetic materials, in particular, have garnered attention due to their ability to be easily recovered through the application of an external magnetic field. In this study, ferrite spinel adsorbents were synthesized by substituting Co(II) into the $FeFe_2O_4$ spinel structure using a coprecipitation method. The random distribution of a Co cation into host $FeFe_2O_4$ compounds, $Fe_{1-x}Co_xFe_2O_4$ (x = 0–1), strongly influenced optical and magnetic properties. Nanoparticle sizes varying within 10–17 nm were obtained in $Fe_{1-x}Co_xFe_2O_4$ compounds. X-ray diffraction and Fourier transform infrared spectroscopy analyses revealed a single-crystal phase that was well fabricated. The optical bandgap energy decreased from 2.27 to 1.89 eV, together with a reduction of magnetic moment from 93.5 to 43.1 emu/g. The $Fe_{1-x}Co_xFe_2O_4$ materials demonstrated significant adsorption performance for Direct Red 79 (DR79), particularly at low pH levels, with optimal results observed at x = 0.5 (FC3). The adsorption behavior was effectively described by the Langmuir and Redlich–Peterson models. Kinetic analysis revealed that the pseudo-second-order and intragranular diffusion models provided the best fit. Thermodynamic analysis indicated an endothermic process (ΔH = 74.947 kJ/mol), suggesting that the adsorption mechanism is primarily physical. This study underscores the potential of $Fe_{1-x}Co_xFe_2O_4$ materials for the effective removal of Direct Red 79 (DR79), offering valuable insights into their synthesis, characterization, and application for environmental remediation. After four cycles of recovery and reuse, the FC3 magnetic nanomaterial was able to remove 42% of the DR79 pollutant while maintaining good chemical stability. The adsorption efficiency of the material for the actual textile wastewater sample reached 57% for color removal and 54.5% for chemical oxygen demand reduction.

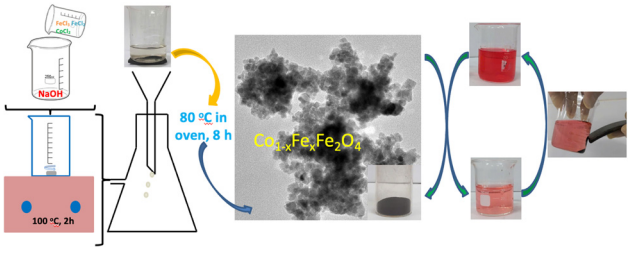

Graphical abstract

Keywords: magnetism, cobalt, spinel, ferrite, co-precipitation

1 Introduction

The issue of water pollution remains a critical global concern, demanding innovative approaches for effective treatment. Various pollutants including dyes used in the textile and leather industries seriously contaminate water sources [1]. Dyes play a crucial role in many industries,

* **Corresponding author: Nguyen Quoc Dung,** Faculty of Chemistry, Thai Nguyen University of Education, 20 Luong Ngoc Quyen, Thai Nguyen City, Thai Nguyen 25000, Vietnam, e-mail: dungnq@tnue.edu.vn
* **Corresponding author: Thi Kim Ngan Tran,** Institute of Applied Technology and Sustainable Development, Nguyen Tat Thanh University, Ho Chi Minh City, Vietnam, e-mail: nganttk@ntt.edu.vn
Vu Thi Hau, Pham Thu Ha, Ngo Thi Mai Viet: Faculty of Chemistry, Thai Nguyen University of Education, 20 Luong Ngoc Quyen, Thai Nguyen City, Thai Nguyen 25000, Vietnam
Pham Hoai Linh: Institute of Materials Science, Vietnam Academy of Science and Technology, 18 Hoang Quoc Viet, Cau Giay, Ha Noi, Vietnam
Nguyen Thuy Chinh: Institute for Tropical Technology, Vietnam Academy of Science and Technology, 18 Hoang Quoc Viet, Cau Giay, Ha Noi, Vietnam; Graduate University of Science and Technology, Vietnam Academy of Science and Technology, 18 Hoang Quoc Viet, Cau Giay, Ha Noi, Vietnam
Dang Duc Dung: Multifunctional Ferroics Materials Laboratory, Faculty of Engineering Physics, Ha Noi University of Science and Technology, 1 Dai Co Viet Road, Ha Noi, Vietnam

particularly in the textile industry, where direct dyes are predominant. They are known environmental pollutants, with approximately 80% of direct dyes being azo compounds that need to be removed from water [2]. Direct Red 79 (DR79), classified as an azo dye, is a synthetic coloring agent extensively used across multiple industries, such as textile, paper, and leather processing. Despite its ubiquity and utility, the environmental ramifications of DR79 are noteworthy. Improper disposal practices can lead to the contamination of aquatic ecosystems, encompassing rivers, lakes, and streams. DR79, alongside other azo dyes, notably exhibits resistance to biodegradation mechanisms, thereby perpetuating the persistence of dye-induced water pollution over extended periods. Numerous methods have been studied for the removal of pollutants, such as photocatalytic degradation [3–7], membrane filtration [8], electrolysis [9], biodegradation [10], precipitation [11], and adsorption [12–15]. Among them, adsorption is highly feasible for practical applications owing to its simplicity, ease of operation, and wide variety of available adsorbent materials that are easy to fabricate [16].

Nanomaterials have large surface area-to-volume ratios and high surface energies, exhibiting strong adsorption capabilities. In particular, nanoparticles can treat pollutants at various depths within water bodies, a feature often overlooked by conventional technologies [14]. Some environment-friendly and cost-effective nanomaterials have been developed and play a crucial role in industrial-pollution remediation, surface-water treatment, groundwater treatment, and drinking water purification. Many materials based on metal oxides such as ZnO [12] and MnO_2/Al_2O_3 [13], as well as magnetic materials like Fe_3O_4 [17,18], ferrites [15], etc., play significant roles in various types of nanoadsorbents. Ferrite nanoparticles used in water and wastewater treatment are highly stable and are easily regenerated without compromising their properties, thereby reducing treatment costs, particularly in terms of recovery [19–21]. Given their magnetic properties, they can also be separated from the environment using an external magnetic field, avoiding the need for centrifugation or complex filtration methods [22–24]. However, Fe_3O_4-based materials often lack stability and tend to undergo phase transition, affecting the magnetic properties of the particles and leading to changes in pollutant-removal efficiency. Hence, substituted-spinel ferrite $Fe_{1-x}M_xFe_2O_4$ (M = divalent metal ion) is increasingly being used for contaminant removal [15]. Additionally, conventional oxides often exhibit poor stability in low pH environments, whereas their adsorption capacity for certain high-color pollutants decreases at low pH and gradually diminishes at high pH for metal-oxide-based adsorbents [25]. Conversely, spinel ferrites remain stable at low pH (pH 2–6) [15,26].

The synthesis of ferromagnetic ferrite materials has garnered significant attention due to their potential applications across various fields, including environmental remediation, catalysis, and energy storage. Among the numerous synthesis techniques – such as [27], sol–gel [28,29], hydrothermal [29,30], solvothermal [30,31] – the co-precipitation method stands out for its simplicity, cost-effectiveness, and ability to produce highly uniform nanoscale particles with tailored properties. This method, in particular, facilitates rapid nucleation at elevated temperatures, enabling the controlled formation of $Fe_{1-x}Co_xFe_2O_4$ ferrites, which are of interest for their magnetic and adsorptive characteristics. For instance, Andersen et al. demonstrated that the rapid growth of $MnFe_2O_4$ and $CoFe_2O_4$ nanocrystals can achieve sizes as small as 10–20 nm [32].

In this study, we employed the co-precipitation method to synthesize $Fe_{1-x}Co_xFe_2O_4$ ferrites, focusing on optimizing their structure for effective adsorption applications. The synthesized materials were tested for their ability to adsorb FDR79, a synthetic dye prevalent in industrial wastewater. The adsorption process was analyzed through various isothermal models, including Langmuir and Redlich–Peterson, to determine the adsorption mechanism and capacity. Additionally, kinetic studies utilizing pseudo-second-order and intragranular diffusion models provided insights into the adsorption dynamics. Our findings indicate that these materials have significant potential for practical application in environmental remediation, particularly in the treatment of dye-contaminated water.

2 Experiment

2.1 Chemicals and instruments

$FeCl_2{\cdot}4H_2O$, $FeCl_3{\cdot}6H_2O$, $CoCl_2{\cdot}6H_2O$, and NaOH powdered chemicals were purchased from Merck. DR79 and acetone were purchased from China. Solutions of 2 M $FeCl_3$, 2 M $FeCl_2$, 2 M $CoCl_2$, 2 M HCl, and 2 M NaOH were prepared from stock chemicals using twice-distilled water. A magnetic heating stirrer (C-MAG HS, IKA) was used for the synthesis of materials. IKA®KS 260 basic and control shakers were used to study adsorption. A pH meter was used to adjust the pH of the solution containing adsorbate. The concentration of adsorbate (DR79) was determined using a UV-1700 spectrophotometer (Shimadzu, Japan).

Table 1: Reagent composition for material preparation

x	2 M $FeCl_2$ (mL)	2 M $FeCl_3$ (mL)	2 M $CoCl_2$ (mL)	2 M HCl (mL)	2 M NaOH (mL)	Denotation of product
0	2	4	0	15	60	F0
0.2	1.6	4	0.4	15	60	FC1
0.4	1.2	4	0.8	15	60	FC2
0.5	1.0	4	1.0	15	60	FC3
0.6	0.8	4	1.2	15	60	FC4
0.8	0.4	4	1.6	15	60	FC5
1	0	4	2	15	60	C0

2.2 Fabrication of $Fe_{1-x}Co_xFe_2O_4$

In the synthesis of Fe_3O_4 nanoparticles, a mixture comprising 2 mL of 2 M $FeCl_2$ and 4 mL of 2 M $FeCl_3$ (resulting in 8 mL of 1 M $FeCl_3$) was combined with 10 mL of 2 M HCl. The resulting mixture was stirred for 1 h at room temperature. Subsequently, 60 mL of 2 M NaOH was brought to a boil at 100°C, and the iron salt solution was swiftly introduced into the boiling NaOH solution. A rapid pouring rate was ensured to secure uniform nucleation of iron salt with NaOH. The reaction was sustained for 1 h at 100°C. Following the reaction, the mixture was filtered, followed by two washes with distilled water until a pH of 7 was reached. The final step involved rinsing the product with acetone.

$Fe_{1-x}Co_xFe_2O_4$ was fabricated similar to that of Fe_3O_4 nanoparticles. However, instead of using $FeCl_2$, a portion of the mixed solution was replaced by $CoCl_2$ in a certain ratio, as shown in Table 1.

2.3 Morphology and structures of materials

The crystal and phase structure, morphology, particle size, and chemical structure of the synthesized samples were characterized by field-emission scanning electron microscopy system (S-4800, Hitachi), X-ray diffraction (XRD) analysis (XRD-Bruker D8 Advance), Fourier transform infrared spectroscopy (FTIR; Nicolet Nexus 670), and ultraviolet–visible diffuse reflectance spectroscopy (UV–Vis-DRS; Hitachi U-2900). Magnetic properties were observed on magnetization plots using a vibrating sample magnetometer (VSM) at room temperature. Specific surface area and pore size were examined through nitrogen adsorption at a low temperature (77.35 K) by using the Brunauer–Emmett–Teller (BET) equation (MicroActive for TriStar II Plus 2.03).

2.4 Adsorption properties

The pH_{pzc} of absorbents was determined as follows. To adjust the pH of 0.1 M NaCl solutions to initial pH values (pH_i) ranging from approximately 3 to 11, 0.1 M HNO_3 and 0.1 M NaOH solutions were prepared. Nine Erlenmeyer flasks with a volume of 250 mL each were filled with 0.02 g of the adsorbent material. Subsequently, 100 mL of the prepared solutions with varying pH_i values were sequentially added to each flask. The mixtures were allowed to stand for 48 h, after which the solutions were filtered, and their pH (pH_f) was measured. The difference between the initial pH (pH_i) and the equilibrium pH (pH_f) was calculated as $\Delta pH = pH_i - pH_f$. A graph illustrating the dependence of ΔpH on pH_i was drawn. The intersection points of the curve with the *x*-axis (where $\Delta pH = 0$) indicated the point of zero charge that needed to be determined.

This study involved the adsorption of DR79 (adsorbate) onto an adsorbent by shaking a conical flask containing the adsorbent in an aqueous solution of the absorbate at 250 rounds per min. The concentration of DR79 was determined using the spectrophotometric method (UV 1700) within the wavelength range of 300–700 nm.

The adsorption capacity was characterized by the adsorption efficiency or removal (%), calculated as the percentage of the adsorbate's concentration at time t (C_t, mg L^{-1}) or equilibrium (C_e, mg L^{-1}) compared with the initial concentration (C_0, mg L^{-1}) according to

$$\text{Removal (\%)} = \frac{C_0 - C_t}{C_0} \times 100, \tag{1}$$

$$\text{Removal (\%)} = \frac{C_0 - C_e}{C_0} \times 100. \tag{2}$$

The adsorption capacity, indicating the amount of adsorbate per unit adsorbent at time t (q_t, mg g^{-1}) or at equilibrium (q_e, mg g^{-1}) in a solution volume V (L) containing m (g) of adsorbent, was calculated by

$$q_e = \frac{(C_0 - C_e)V}{m}, \tag{3}$$

$$q_t = \frac{(C_0 - C_t)V}{m}. \tag{4}$$

In theory, depending on the adsorption system comprising adsorbent, adsorbate, and the adsorption environment, the dependence of adsorption capacity on concentration at equilibrium at a specific temperature follows different laws determined by the isothermal adsorption equation. The use of various isotherms such as Langmuir, Freundlich, Temkin, and Redlich–Peterson is common in analyzing adsorption phenomena.

The Langmuir single-layer homogeneous adsorption model in linear form, with a maximum adsorption capacity (q_{max}) and Langmuir adsorption constant (K_L), is represented by

$$\frac{C_e}{q_e} = \frac{1}{q_{max}K_L} + \frac{C_e}{q_{max}}. \quad (5)$$

In the Freundlich adsorption isotherm, an empirical adsorption model, the adsorbate forms a monomolecular layer on the surface of the adsorbent for a linear curve by

$$\ln q_e = \ln K_F + \frac{1}{n}\ln C_e, \quad (6)$$

where K_F is the Freundlich adsorption constant, and n is a constant ($n > 1$).

The Temkin isotherm model indirectly explores the influence of interactions between adsorbent and adsorbate under the assumption that the heat of adsorption for all molecules in a layer decreases linearly with increased surface coverage of the adsorbent. The Temkin isotherm model is mathematically expressed by

$$q_e = \frac{RT}{b_T}\ln K_T + \frac{RT}{b_T}\ln C_e, \quad (7)$$

where K_T (L mol^{-1}) is the equilibrium binding constant, b is related to the adsorption heat, R is the universal gas constant (8.314 J K^{-1} mol^{-1}), and T is the temperature (K).

The Redlich–Peterson isotherm is a combination of the Langmuir and Freundlich isotherms. It adopts the numerator from the Langmuir isotherm and offers the advantage of accessing the Henry region at infinite dilution. This isotherm model is an empirical three-parameter model, incorporating elements from the Langmuir and Freundlich equations; thus, the adsorption mechanism is a mixture and does not adhere to ideal single-layer adsorption. The linear form of the Redlich–Peterson equation is shown as follows:

$$\ln\frac{C_e}{q_e} = \beta \ln C_e - \ln A, \quad (8)$$

where A is the Redlich–Peterson isotherm constant (L g^{-1}), and β is an exponent between 0 and 1 [33].

3 Results and discussion

3.1 Morphology and structure of materials

The morphology and size of the Co-substituted Fe_3O_4 nanoparticles were studied through field emission scanning electron microscope (FESEM) and transmission electron microscopy (TEM) images, as shown in Figures 1 and 2. It can be seen that all samples exhibit a nearly cubic shape

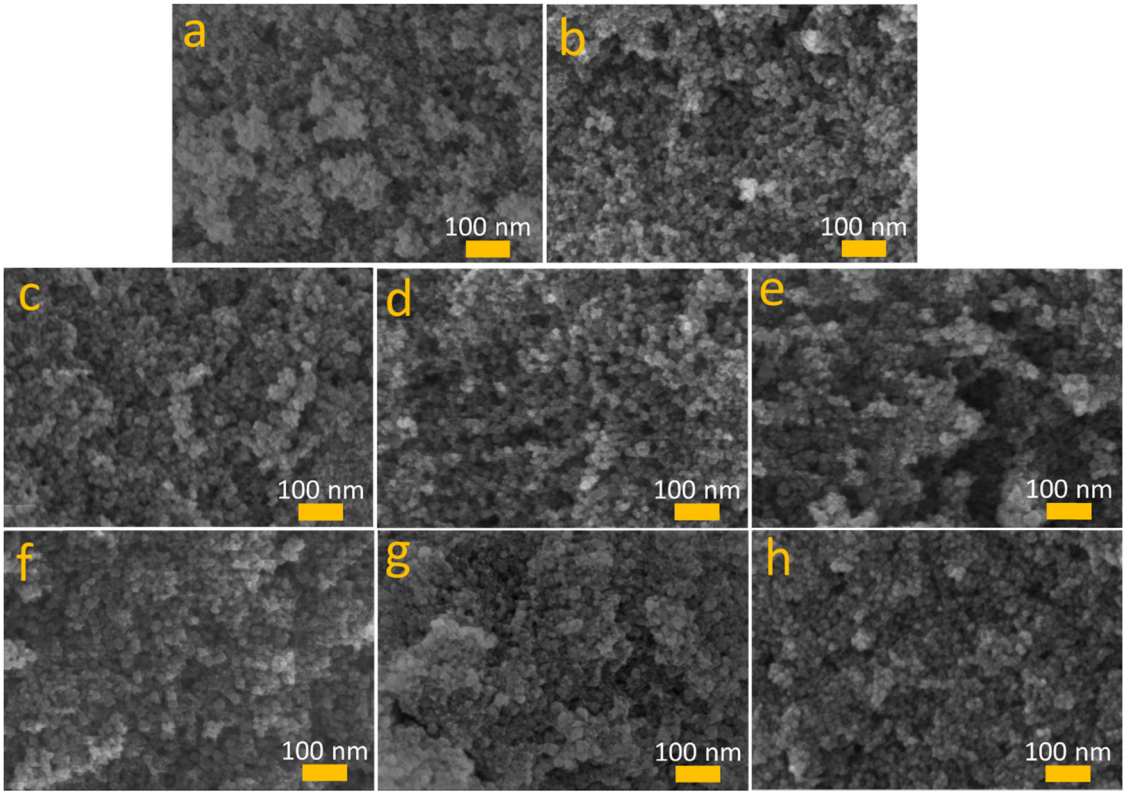

Figure 1: FESEM images of (a) F0, (b) FC1, (c) FC2, (d) FC3, (e) FC4, (f) FC5, (g) C0, and (h) FC2 recovered after adsorption.

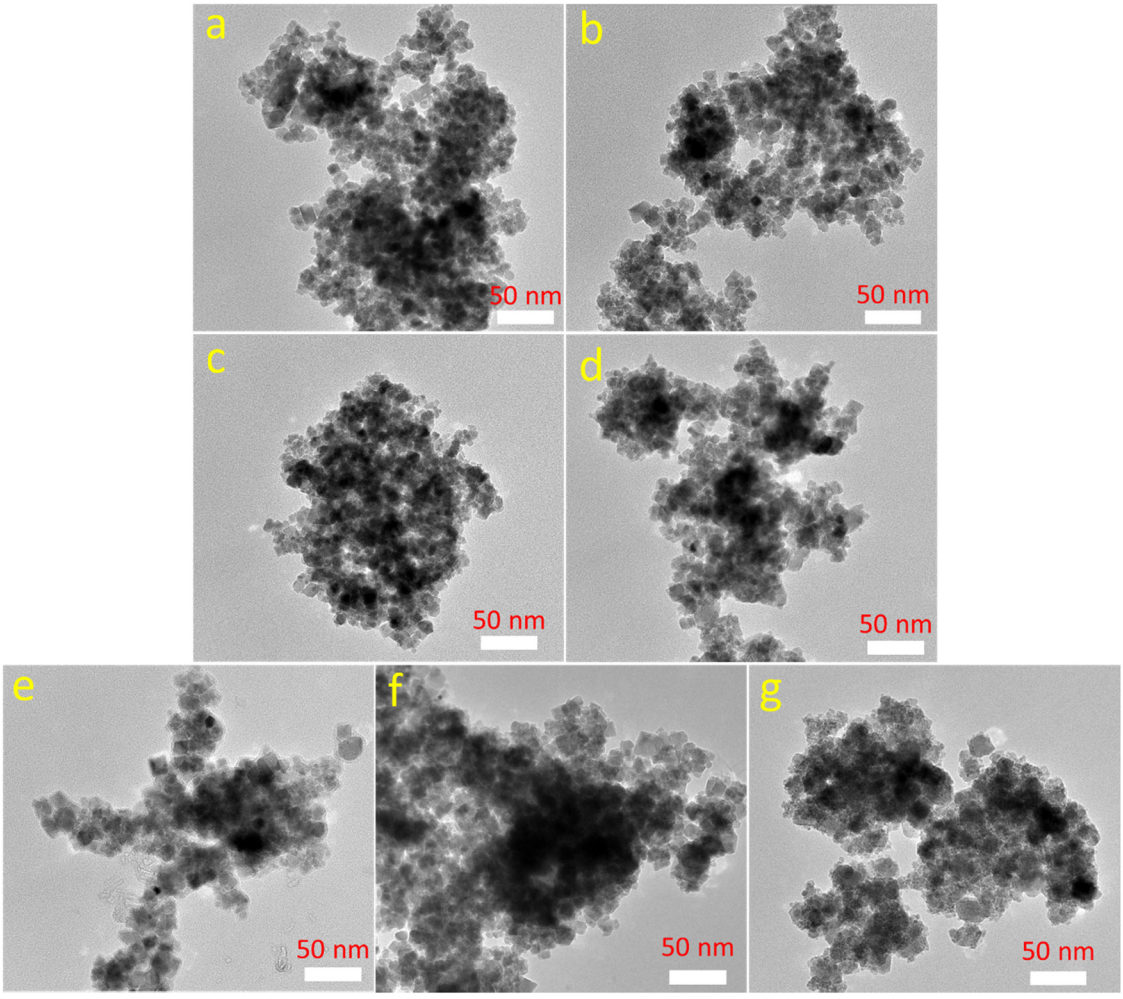

Figure 2: TEM images of (a) F0, (b) FC1, (c) FC2, (d) FC3, (e) FC4, (f) FC5, and (g) C0.

with a small size in the range of 7–25 nm, with the average size depending on the Co-substituted concentration. The ImageJ software was used to estimate the average size and the particle-size distribution of the obtained samples. The results reveal that the average size of the Co-substituted Fe_3O_4 nanoparticles increases with increasing the Co-substituted content, ranging from approximately 10 nm at F0 to 17 nm at C0 (Figure 3).

The phase and crystalline structure of the as-prepared samples were analyzed by the XRD patterns, as presented in Figure 4(a). The XRD pattern of F0 shows the diffraction peaks at 2θ of 29.81°, 35.13°, 42.98°, 56.81°, and 62.52°, corresponding to the (220), (311), (400), (422), and (511) crystal planes belong to a cubic spinel structure of Fe_3O_4 (JCPDS # 01-086-1347c), respectively.

The Scherrer equation was applied to determine the crystallite size based on the most intense diffraction peak (311), as shown in the following equation:

$$t = \frac{k\lambda}{\beta \cos\theta}, \tag{9}$$

where k is a dimensionless shape factor (k = 0.9), λ is the X-ray wavelength (CuKa = 1.5405 Å), β is the full width at the half-maximum of the (311) diffraction peak, and θ is the angle of diffraction ($2\theta/2$). The results are presented in Table 2. For the Co-substituted Fe_3O_4 nanoparticles, no new diffraction peaks were detected, and the existing diffraction peaks slightly left shifted, indicating Co(II) ions effectively replaced the Fe(II) ions in the Fe_3O_4 structure to form $Co_xFe_{1-x}Fe_2O_4$ nanoparticles. Moreover, the obtained results from Table 2 also reveal that with increased Co content, the crystal size of the nanoparticles gradually increased initially (for x = 0, 0.2, 0.4, and 0.5), followed by a rapid escalation from x = 0.6 to 1. This trend was consistent with observations from the TEM image analysis presented earlier. The findings from

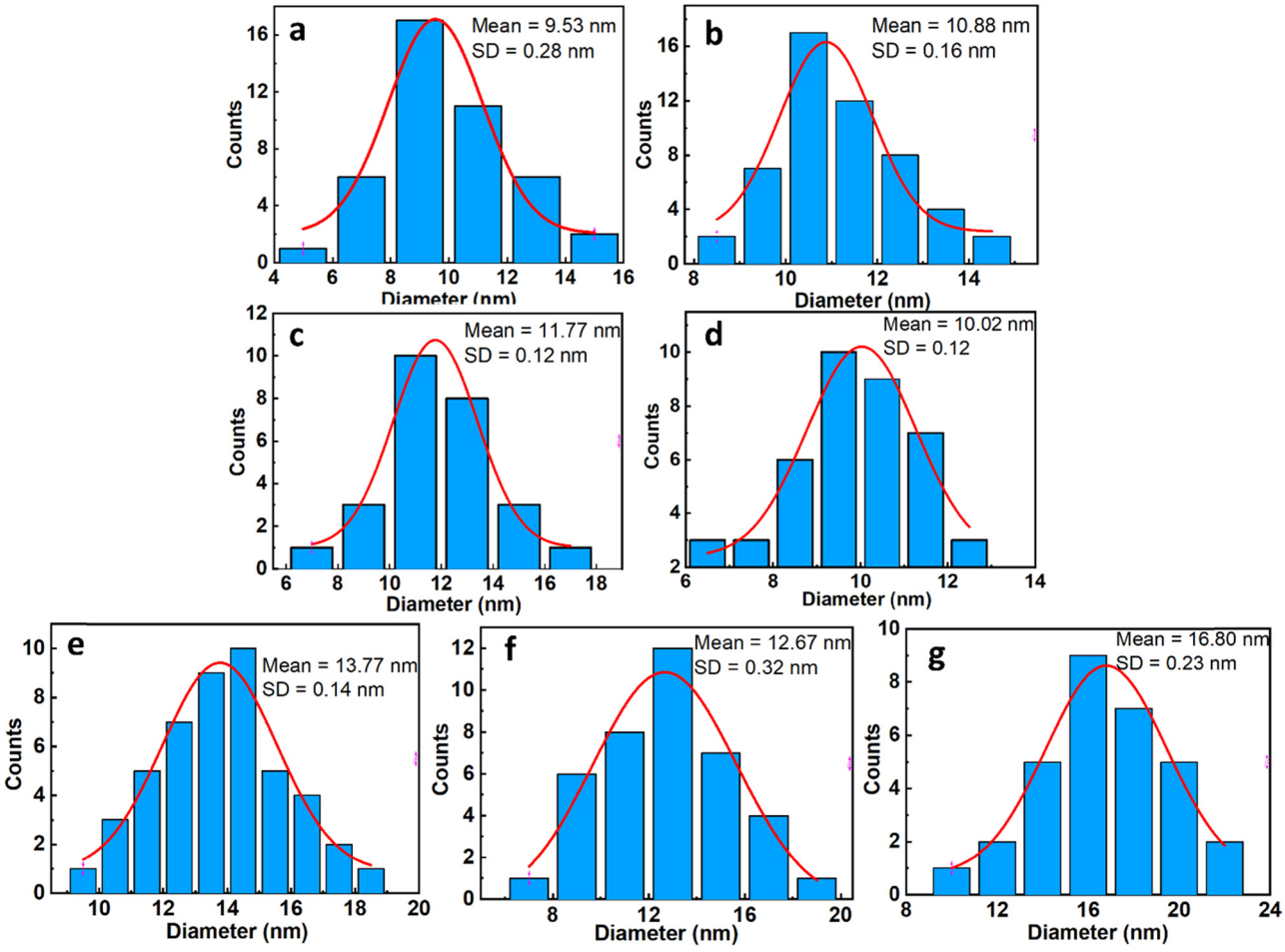

Figure 3: Size distribution of (a) F0, (b–f) FCn, and (g) C0.

TEM and XRD analyses may be due to the discrepancy in size between the trivalent(III) and divalent(II) oxidation states, specifically Co(II) and Fe(III) in the materials, compared with Fe(II) and Fe(III) in Fe_3O_4. The incorporation of Co(II) into Fe(II) sites induced lattice distortion, which expanded the crystal size.

The FTIR spectra of the as-prepared samples are shown in Figure 4(b). All samples exhibited similar spectral peaks around 3,200–3,400 cm^{-1}, attributed to the presence of hydroxyl groups on the surface of the nanoparticles, likely influenced by moisture [34]. Two main stretching vibration bands corresponding to metal–oxygen bonds, ν_1 and ν_2, were characteristic of spinel materials. ν_1 corresponded with intrinsic stretching vibrations of the metal at the tetrahedral site, $M_{tetra} \leftrightarrow O$. ν_2 was assigned to octahedral-metal stretching $M_{octa} \leftrightarrow O$ of Fe(III) with O [35]. ν_1 shifted by about 610–569 nm from F0 to C0, indicating the replacement of Fe(II) by Co(II).

Figure 4(c) illustrates the FTIR spectra of DR79 and FC3 samples before and after DR79 adsorption. New peaks belonging to vibration bands of DR79 are observed in the FTIR spectrum of FC3 after DR79 adsorption compared to that of the FC3 sample. For instance, the band at 1,052 cm^{-1} reflects the C–O stretch vibration in DR79, and the peaks at 1,194 cm^{-1} (strong peak) and 1,225 cm^{-1} (shoulder peak) correspond to the symmetric and asymmetric vibrations of O═S═O in DR79. Additionally, the 1,109 cm^{-1} band observed in DR79 is attributed to the S–O stretching vibration, while in FC3-DR79, this vibration shifts to 1,124 cm^{-1}, indicative of an interaction between −S−O and the metal ion present in FC3. Notably, the peak at 1,225 cm^{-1} in DR79 shifts to 1,229 cm^{-1} (weak peak) in FC3, potentially due to the linkage between O═S═O and the metal ion in FC3. Peaks at 1,272 cm^{-1}, characteristic of C–N stretching in the structure of DR79, are also observed in FC3-DR79. These results confirm that DR79 was adsorbed onto FC3,

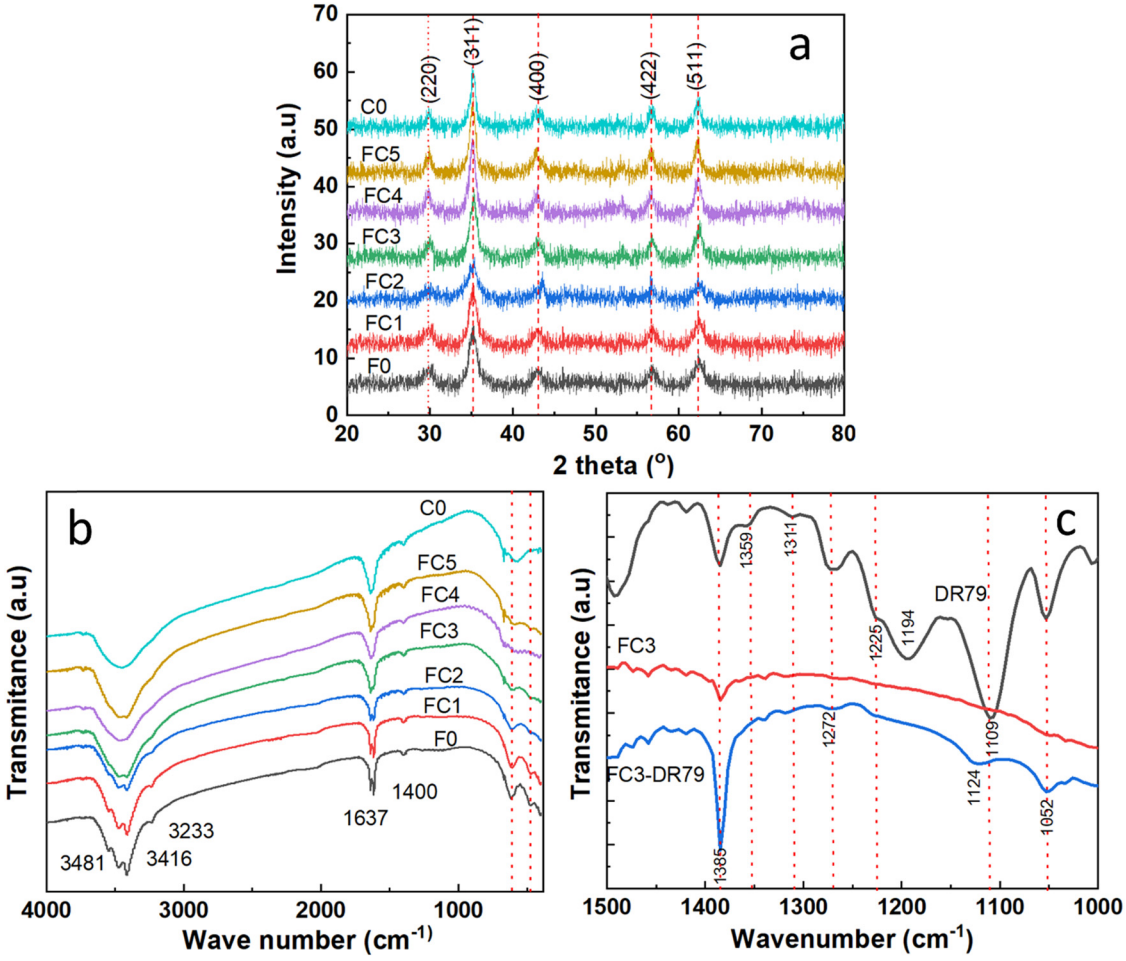

Figure 4: (a) XRD pattern of F0, FCn (n = 1–5), and C0. (b) FTIR spectrum of F0, FCn (n = 1–5), and C0. (c) FTIR spectrum of DR79, FC3 and DR79 adsorption.

Table 2: Determination of crystal size using the Scherrer equation

Samples	F0 (x = 0)	FC1 (x = 0.2)	FC2 (x = 0.4)	FC3 (x = 0.5)	FC4 (x = 0.6)	FC5 (x = 0.8)	C0 (x = 1)
Particle size (nm)	6.61	6.58	6.60	6.96	8.44	8.96	9.93

primarily through interactions with the $-SO_3^-$ group on DR79 and the FC3 surface.

The impact of Co(II) substitution on the energy-band structure, as assessed using UV–Vis-DRS measurements, is depicted in Figure 5(a). A red shift accompanied by multiple absorption peaks (e.g., ~475 and 669 nm) was found in the absorption edge. This finding indicated a reduction in the bandgap width (E_g) values and the presence of multiple absorptions owing to Co(II) substitution at the Fe(II) site. Recent studies have suggested that the energy-band structures of these materials undergo direct bandgap transitions. Utilizing the Wood–Tauc method to determine the bandgap width, the material was identified as a direct semiconductor, thereby establishing the dependence of $\alpha h\upsilon^2$ on $h\upsilon$, as illustrated in Figure 5(b–h). In this equation, α, h, and υ represent the absorbance coefficient, Planck constant, and frequency, respectively. The bandgap energy was extrapolated from the linear portion intersecting the horizontal axis. These results demonstrated a reduction in bandgap energy with progressive substitution of Fe(II) by Co(II), decreasing rapidly from x = 0 to x = 0.5, followed by a slow or nearly negligible decrease from x = 0.6 to x = 1, as depicted in Figure 5(i). Hence, Co(II) substitution at the Fe(II) site decreased the bandgap width.

The field-dependent magnetization curves were obtained at room temperature of all samples shown in Figure 6(a), further confirming the ferromagnetic behavior of the nanoparticles at room temperature. The influence of Co content on the magnetic properties of Fe_3O_4 nanoparticles is shown in Figure 6(b). It can be seen that the

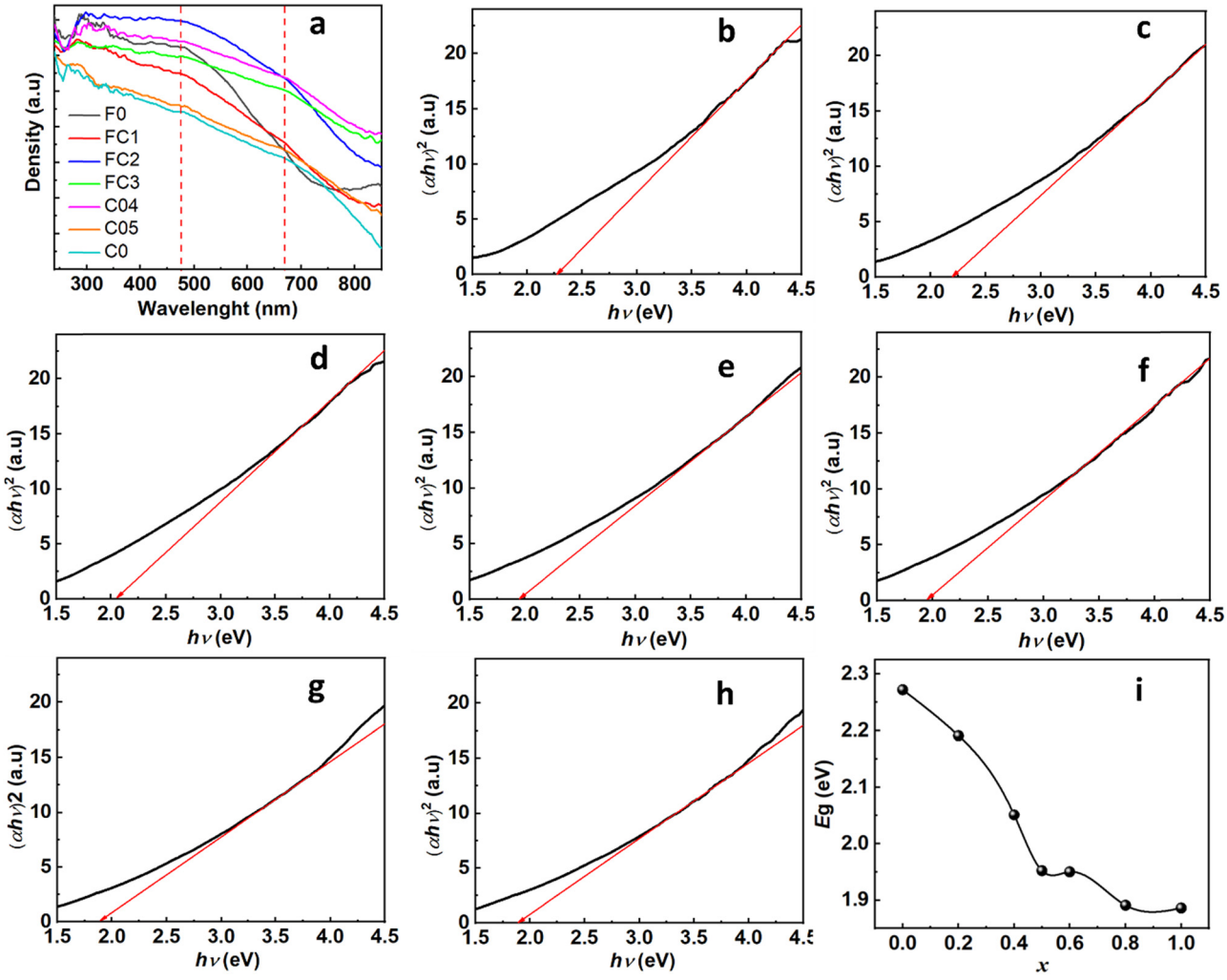

Figure 5: (a) UV–Vis-DRS spectra of F0, FCn, and C0. (b–h) Determination of optical band gap energy (E_g) values of F0, FCn, and C0 using the Wood–Tauc method. (i) Plot of E_g values of F0, FCn, and C0 vs *x*.

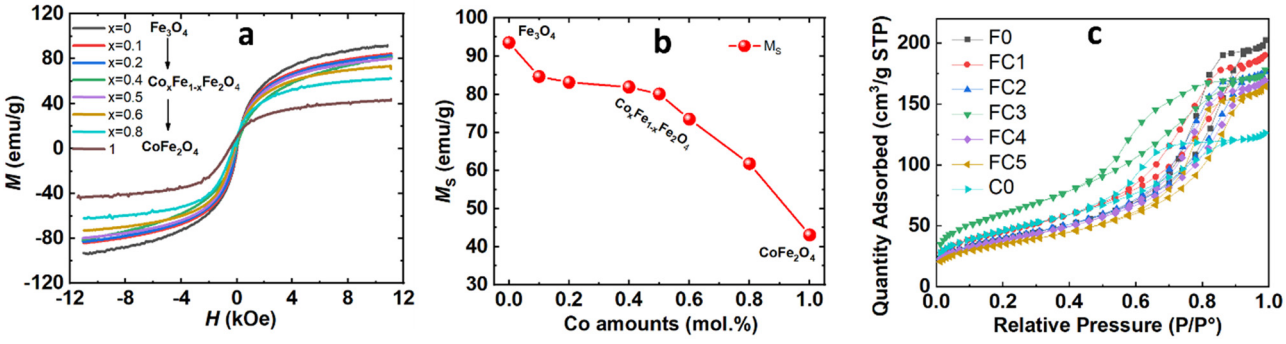

Figure 6: (a) Magnetic hysteresis loops of F0, FCn, and C0; (b) plot of M_S vs F0, FCn, and C0; and (c) N_2 – adsorption/desorption isotherms of F0, FCn, and C0.

saturation magnetization (M_S) of the nanoparticles decreased when increasing the Co substituted content. Interestingly, for Co amounts below 50 mol%, the M_S values of the nanoparticles decreased slowly and rapidly reduced for Co amounts over 50 mol%. The M_S values obtained were around 93.5 emu/g for the Fe_3O_4 sample and decreased to 43.1 emu/g for the complete replacement of 1 Fe cation via 1 Co cation to form a $CoFe_2O_4$ composition. Our observation results were consistent with the recently reported magnetic properties of $Co_xFe_{1-x}Fe_2O_4$ in nanoparticles. The magnetic moments depend on the amounts of Co substitution in Fe_3O_4 and are also strongly affected by crystal size [34,36–38]. Sangsuriyonk et al. [34] reported that the M_S values of $CoFe_2O_4$ ranged within around 46.19–28.06 emu/g, which strongly depended on the surfactant templates, resulting in changed particle sizes from 42 to 16 nm. Similarly, the M_S values of $CoFe_2O_4$ compounds are reportedly around 34.70 to 74.08 emu/g, which strongly depend on the nanograin size [36–38]. The nanograin size of Fe_3O_4 also affected the M_S values, ranging from 63.36 to 100.41 emu/g [34,36–38]. Sangsuriyonk et al. suggested that the reduction of M_S values of $Co_xFe_{1-x}Fe_2O_4$ samples results from different magnetic moments of Co^{2+} (3.87 magnetons) and Fe^{2+} (4.09 magnetons) [34]. Sathya et al. [39] reported that particle size more strongly affects the magnetic moment than does the effect of cobalt content in $Co_xFe_{3-x}O_4$ compounds. Biswal et al. reported that the M_S values of $CoFe_2O_4$ nanoparticles are affected by the molar ratios of Fe^{2+} to Co^{2+} ions, with M_S values of 90 emu/g at 75:25 molar ratios of Fe^{2+} to Co^{2+} and a particle size of 13 nm [40]. Our TEM results exhibited that the samples' nanograin size ranged between 10 and 17 nm. We suggested that the magnetic moment strongly depends on the nanograin size and the magnetic moment compensation between Co and Fe cations within the $FeFe_2O_4$ crystal structure during substitution to form as single phase.

The properties related to porosity and surface area of the materials were determined from the adsorption–desorption isotherms of nitrogen using the BET method. Figure 7 illustrates that the adsorption–desorption isotherms of F0, FCn, and C0 fell under type IV and H-type, which were characteristic of mesoporous materials.

Surface area, pore volume, and pore diameter are listed in Table 3. Results indicated significantly large specific surface areas for the materials, with the highest observed in FC3. The pore size and volume suggested that the materials had average mesopore size, promising good adsorption capabilities.

3.2 Adsorption of $Co_xFe_{1-x}Fe_2O_4$ onto DR79

3.2.1 Selection of $Co_xFe_{1-x}Fe_2O_4$

A preliminary investigation was conducted to select the material with the appropriate value of x for studying the adsorption properties of the material. We determined the adsorption efficiency of 0.02 g of material for DR79 in a 25 mL solution with a concentration of 50 mg/L at pH 3 with a sample shaking rate of 250 rpm. As shown in Figure 7(a), FC3 (x = 0.5) exhibited the highest adsorption efficiency. Therefore, FC3 was chosen to investigate the adsorption properties for subsequent experiments.

3.2.2 Effect of initial pH

The determination of the isoelectric point of the ferrite material is depicted in Figure 7(b). The isoelectric point was defined as the intersection of the $\Delta pH - pH_i$ curve with the pH_i axis, yielding a value of 6.1. This finding indicated that below a pH of 6.1, the material surface was negatively charged, and above a pH of 6.1, the material surface was positively charged. At pH 6.1, the material surface was neutral.

The adsorption efficiency of DR79 dye within the pH range of 3–11, with an initial concentration of 50 mg/L in a volume of 25 mL, is depicted in Figure 7(c). The adsorption efficiency of DR79 dye onto ferrite highly depended on pH. Approximately 79.13% of the dye was adsorbed at pH 3, whereas the amount of dye adsorbed decreased with increased pH, reaching an adsorption efficiency of 7.5% at pH 11.

This finding can be explained as follows. With decreased pH, the concentration of H^+ ions in the environment increased, facilitating electrostatic interaction with the negatively charged DR79 dye molecules, allowing them to adhere to the surface of ferrite and creating favorable conditions for adsorption. Conversely, with increased pH, the concentration of OH^- ions increased, resulting in the surfaces of the adsorbent material becoming more negatively charged. In this scenario, repulsive forces dominated between the ferrite and DR79 dye molecules. Additionally, owing to the excess OH^- ions in the solution, competitive adsorption occurred between the anionic DR79 dye molecules and OH^- ions, reducing the adsorption efficiency. Therefore, pH 3 was selected for subsequent experiments.

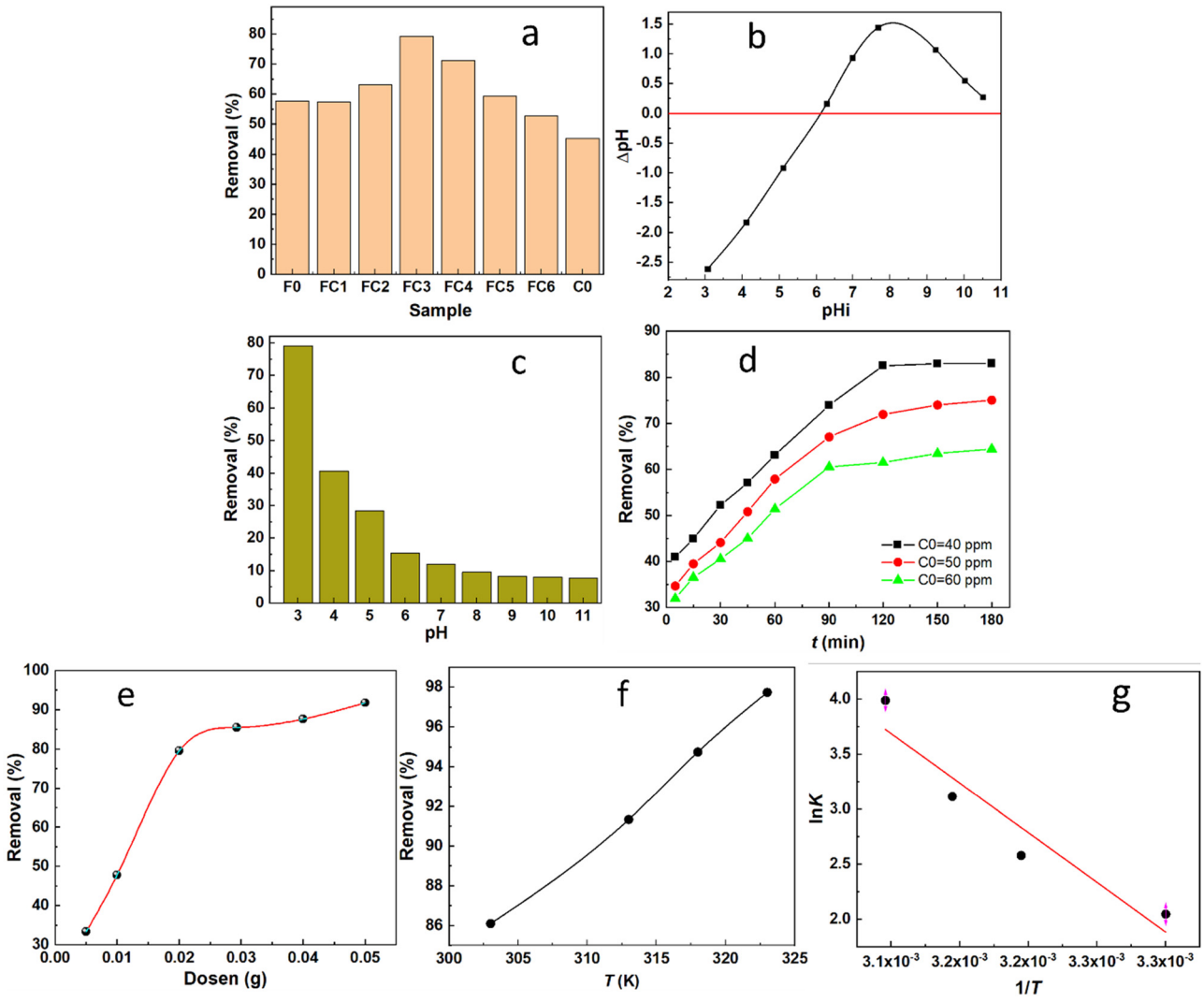

Figure 7: (a) Removal (%) of DR79 on different materials (F0, FCn, and C0); (b) determination of FC3's isoelectric point; (c) adsorption efficiency of FC3 to DR79 at different pH values from 3 to 11; (d) effect of contact time on DR79 adsorption (FC3 mass of 0.02 g, pH 3, shake speed of 250 rpm, temperature of 25°C; (e) effect of adsorbent dose on the adsorption of DR79 (V = 25 mL, pH 3, 250 rpm, 25°C); (f) adsorption efficiency of FC3 to DR79 (C_0 = 50 mg/L, pH 3) at different temperatures; and (g) plot of ln$K$ vs 1/T.

Table 3: Parameters in BET adsorption of materials

Samples	BET area (m^2/g)	Pore volume (cm^3/g)	Pore size (nm)
F0	142.2478	0.309	8.9639
FC1	165.5367	0.285394	7.3799
FC2	143.6720	0.265636	7.8945
FC3	217.9623	0.263953	5.0186
FC4	139.3112	0.254646	7.8998
FC5	126.1336	0.247761	8.5075
C0	167.1040	0.181129	4.9022

3.2.3 Effect of contact time

Figure 7(d) illustrates the dependence of DR79 adsorption efficiency on contact time at various DR79 concentrations, and all materials had a consistent trend. Specifically, within the observation period ranging from 5 to 180 min, the adsorption efficiency increased relatively rapidly from 5 to 120 min and approached linearity. Subsequently, it stabilized gradually between 120 and 180 min. This finding can be explained as follows. Initially, adsorption occurred rapidly owing to the availability of vacant adsorption sites

on the adsorbent surface. After 120 min, adsorption slowed down because the number of available adsorption sites decreased. In other words, adsorption had sufficient time to reach equilibrium. Therefore, an adsorption time of 120 min was used to study the processes related to adsorption equilibrium.

3.2.4 Effect of adsorbent dose

Figure 7(e) shows that the adsorption efficiency of DR79 increased with an increased dose of FC3. In the investigated FC3 mass range from 0.005 to 0.05 g, the adsorption efficiency of DR79 increased from 33.33 to 91.75%. This finding was due to the larger surface area, increased number of adsorption sites, and a larger number of surface functional groups. Adsorption efficiency increased linearly with increased FC3 mass from 0.005 to 0.02 g and then increased slowly. Therefore, we chose an FC3 mass of 0.02 g (or an adsorption dose of 0.8 g/L) for subsequent experiments.

3.2.5 Effect of adsorption temperature

Figure 7(f) shows that with increased temperature, the adsorption efficiency also increased. At various temperatures, the adsorption efficiency of DR79 on ferrite was found to be 86.09% at 303 K, 91.34% at 313 K, 94.74% at 318 K, and 97.73% at 323 K. The increased adsorption efficiency of DR79 on ferrite with increased temperature can be explained as follows. The adsorption of DR79 onto ferrite was endothermic. With increased temperature, the adsorption equilibrium shifted forward, reducing the adsorbate concentration in the solution. The outcome was enhanced adsorption capacity of the process.

3.2.6 Adsorption-isotherm models

All adsorption isotherms investigated are depicted in Figure 8, and the calculated constants and correlation coefficients derived from these plots are presented and compared in Table 4, which also illustrates the model

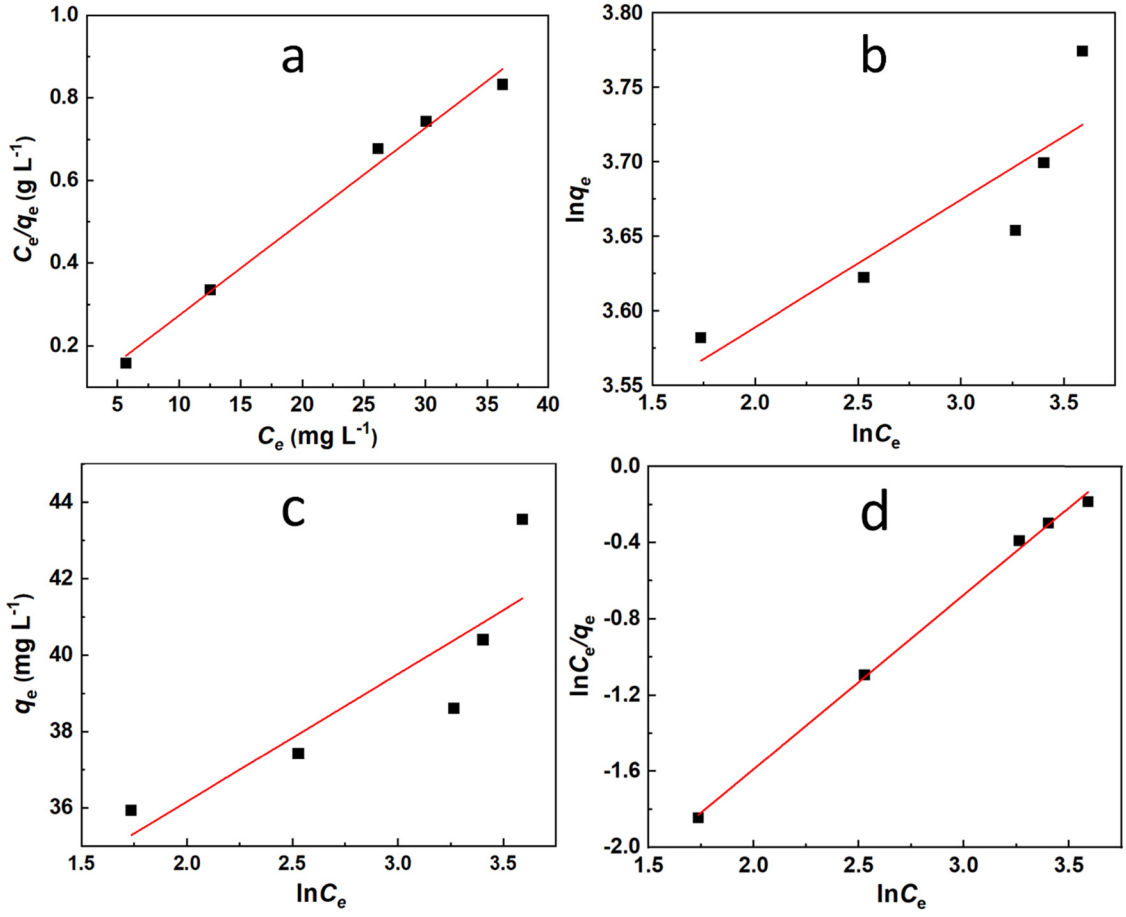

Figure 8: Representation of adsorption-isotherm models: (a) Langmuir, (b) Freundlich, (c) Temkin, and (d) Redlich–Peterson.

Table 4: Experimental parameters from adsorption-isotherm models

Langmuir	q_{max} (mg g^{-1})	K_L	R_L	R^2
	44.07	0.4819	0.0288	0.9901
Freundlich	K_F	*1/n*		R^2
	30.51	0.0854		0.7831
Temkin	A_T (L g^{-1})	*B*	b_T (kJ mol^{-1} K^{-1})	R^2
	6838.774	3.3395	741.889	0.7594
Redlich–Peterson	β	*A* (mg L^{-1})		R^2
	0.9146	30.5144		0.9976

parameters of the DR79 adsorption isotherm on FC3. Comparing the correlation coefficients, the Langmuir [Figure 8(a)] and Redlich–Peterson [Figure 8(d)] isotherm models were the most appropriate for the experimental data, with $R^2 > 0.99$. The maximum adsorption capacity determined by the Langmuir isotherm model was 44.07 mg g^{-1}. The Freundlich [Figure 8(b)] and Temkin [Figure 8(c)] isotherm models exhibited considerably lower R^2 values (0.7831 and 0.7594, respectively), indicating poor fits of the experimental data to these two models. The adsorption capacity of ferrite and other adsorbents for various types of anionic dyes is compared in Table 6 [26,41–49].

3.2.7 Adsorption kinetics

The adsorption kinetics of the material were investigated by analyzing its adsorption capacity over time, as depicted in Figure 7(d). Various kinetic models, including pseudo-first-order, pseudo-second-order, intraparticle diffusion, and Elovich, were studied and are illustrated in Figure 9(a–d). The parameters determined from the pseudo-first-order, pseudo-second-order, intraparticle diffusion, and Elovich kinetic models are presented in Table 5. The values of k_1 and k_2 were calculated from the plots of $\log(q_e - q_t)$ versus t and t/q_t versus t, respectively, as depicted in Figure 9(a) and (b), respectively. Comparing the correlation coefficients (R^2) for all kinetic models in Table 5 revealed that the pseudo-second-order kinetic model was the most suitable. The correlation coefficients for the pseudo-second-order kinetic model ($R^2 \geq 0.983$) were higher than those for the pseudo-first-order ($R^2 \leq 0.9814$) and Elovich models ($R^2 \leq 0.9319$), as well as the intraparticle diffusion model. The intragranular diffusion model exhibited a substantial R^2 of ≥0.9663, indicating that the adsorption kinetics of the system partially conformed to this model as well. The values of k_{id} were obtained from the slope of the linear plot of q_t versus $t^{0.5}$ from Figure 9(c). The intercept for this plot was not equal to 0, meaning that intraparticle diffusion was not solely rate-limiting.

Comparison with some adsorption systems of the material for anionic dye reported in some literature demonstrated the excellent adsorption capacity of the material. The equilibrium adsorption model and the kinetic adsorption model were consistent with previous studies Table 6.

3.2.8 Adsorption thermodynamic

Variations in the thermodynamic parameters, namely, free energy (ΔG^0), enthalpy (ΔH^0), and entropy (ΔS°), of the adsorption process were calculated using the following equations:

$$K_D = \frac{q_e}{C_{cb}}, \tag{10}$$

$$\Delta G^0 = -RT \ \ln K_D, \tag{11}$$

$$\ln K_D = -\frac{\Delta G^0}{RT} = -\frac{\Delta H^0}{RT} + \frac{\Delta S^0}{R}, \tag{12}$$

Table 5: Parameters and constants obtained from the kinetic models

	First-order kinetic			Second-order kinetic		
C_o (mg L^{-1})	q_e (mg g^{-1})	k_1 (min^{-1})	R^2	q_e (mg g^{-1})	k_2 (min^{-1} L mg^{-1})	R^2
40	46.6767	0.040993	0.8526	51.8135	0.000112268	0.9902
50	33.3811	0.023260	0.9814	50.2513	0.000147712	0.9859
60	34.4191	0.026715	0.9597	45.6621	0.000172708	0.9830
	Intragranular diffusion			**Elovich**		
	k_{id}	*C*	R^2	α	β	R^2
40	2.2645	15.39	0.9664	23.93317	0.162999	0.8493
50	2.7190	13.87	0.9773	13.23777	0.125560	0.9137
60	2.7778	16.05	0.9663	6110.2921	0.346332	0.9319

Table 6: Comparison of some adsorption parameters of the material with those reported in previous studies

Adsorbent	Adsorbant	q_{max} (mg g^{-1})	Isothermal adsorption model/kinetic model	Ref.
Spent tea leaves (modified polyethyleneimine)	Reactive Black 5	71.9	Temkin/pseudo-second-order	[41]
Nerium oleander flower (activated carbon)	Direct turquoise blues	33.3	Langmuir and Freundlich/pseudo-second-order	[42]
Cassava root husk	Direct Black ECO TFA	46.1	Langmuir/pseudo-second-order	[43]
Rice husk	Direct red 31	25.63	Langmuir/pseudo-second-order	[44]
	Direct Orang 26	19.96		
Clay	Direct Red 243	156.25	Langmuir/pseudo-second-order	[26]
Canola hul	Reactive 198	2.8	Temkin/pseudo-second-order	[45]
	Reactive Blue 19	2.0		
	Direct red 79	3.1		
	Direct red 80	8.7		
Orange Pell	Direct red 79	151.5	Langmuir and Freundlich/pseudo-second-order	[46]
	Direct Yellow 27	153.85		
Powdered tourmaline	Direct red 23	153	—	[47]
$Fe_xCo_{3-x}O_4$	Congo Red	128.6	Langmuir and Freundlich/pseudo-first-order	[48]
Commercial MCC	Reactive Blue 21	30	Langmuir/pseudo-second-order	[49]
FC3	Direct Red 79	44.07	Langmuir, Redlich-Petorson/pseudo-second-order, intragranular diffusion	This work

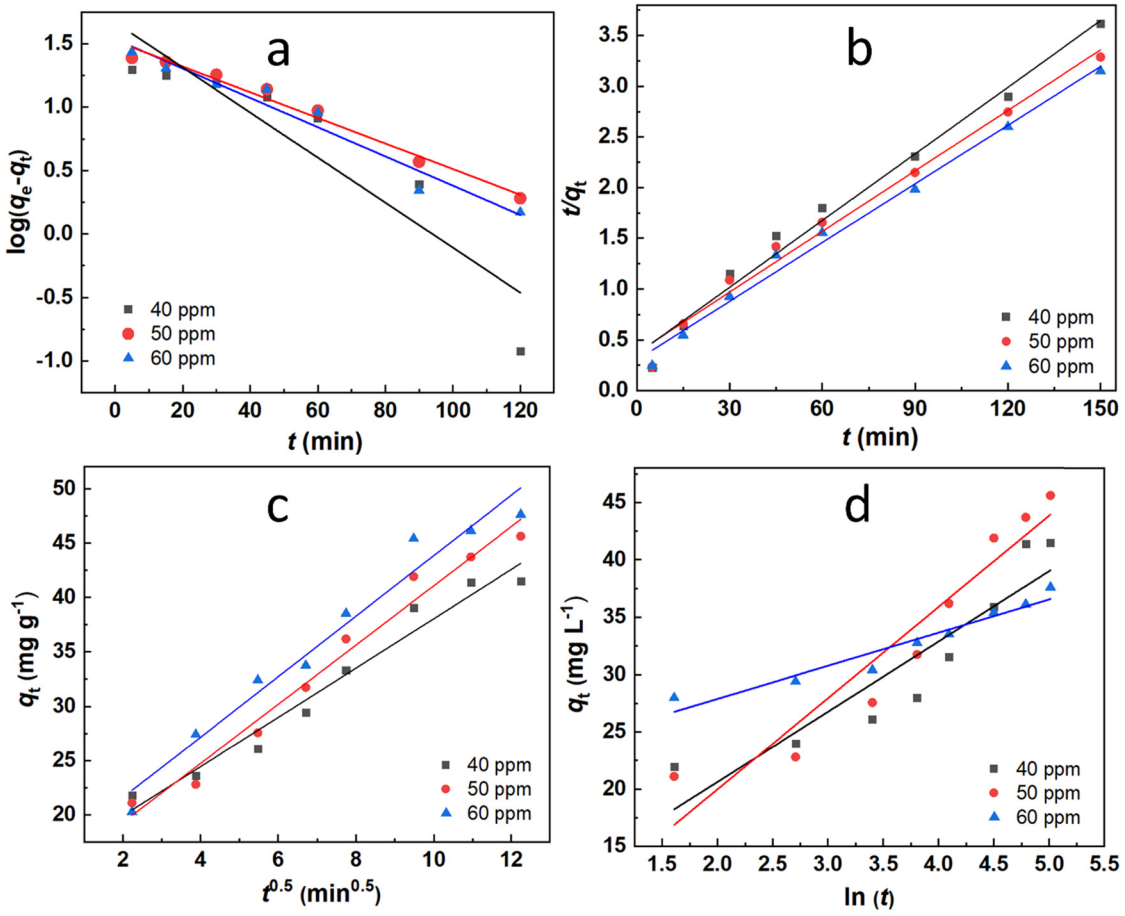

Figure 9: Plots of kinetic adsorption models: (a) pseudo-first-order, (b) pseudo-second-order, (c) intraparticle diffusion, and (d) Elovich.

Table 7: Thermodynamic parameters of adsorption

T (K)	$\Delta G°$ (kJ/mol)	$\Delta H°$ (kJ/mol)	$\Delta S°$ (kJ/mol K)
303	−5.155	74.947	0.263
313	−6.711		
318	−8.235		
323	−10.706′		

where K_D is the equilibrium constant, R is the gas constant, and T is the temperature in Kelvin scale.

The linear relationship between $\ln K_D$ and $1/T$ Figure 7(g) allows for the determination of thermodynamic quantities, with the results presented in Table 7. The values of variation in free energy (ΔG^0) determined ranged from −5.155 to −10.706 kJ/mol, and the entropy variation (ΔS^0) was 0.263 kJ/mol. This finding indicated that the adsorption of DR79 onto ferrite was spontaneous. The calculated enthalpy variation (ΔH^0) was 74.947 kJ/mol, demonstrating that the adsorption process was endothermic. In adsorption processes, when ΔH^0 <25 kJ/mol, Van Der Waals forces are the main factor for physical adsorption. If ΔH^0 = 40–200 kJ/mol, chemical bonding predominates, leading to chemical adsorption.

3.2.9 Comparison of the FC3 performance with other adsorbents and real wastewater

In Table 8, the organic matter removal efficiency of FC3 nanoparticles is comparable to other adsorbents [43,47,50–55], while the dosage used is very small and the treatment time is relatively short.

To evaluate the effectiveness of the real wastewater treatment process, we conducted UV–Vis spectroscopy scans and determined the chemical oxygen demand (COD) values of the wastewater samples before and after treatment. In this study, the textile dyeing wastewater samples were collected from a traditional dyeing village in Ha Dong district, Hanoi, Vietnam. The color of the textile dyeing wastewater could involve various dyes, so we performed UV–Vis scans on the red-colored wastewater samples before and after 120 min of adsorption by FC3, as shown in Figure 10(e). The results indicated that the actual red-colored wastewater sample exhibited a single maximum absorption wavelength at λ = 510 nm. The adsorption efficiency of the red-colored wastewater sample before and after 120 min of adsorption by FC3 was 57%.

COD is an important method for measuring the concentration of organic substances in wastewater solutions, determining the total amount of oxygen required to oxidize the organic dyes into CO_2 and water [56]. This implies that a low COD value indicates high organic matter treatment (adsorption) efficiency. Conversely, a high COD value reflects a significant oxygen demand to oxidize the remaining organic substances after the adsorption process.

After 120 min of adsorption, the COD of the wastewater decreased from 406.67 to 185 mg/L, achieving a COD removal efficiency of 54.5%. Notably, this COD value fell below the WHO's permissible limit of 200 mg/L for wastewater, demonstrating the potential of FC3 in removing dyes through the adsorption process.

Table 8: Comparison of FC3 with other adsorbents

Adsorbent	Dye	Initial concentration of dye (ppm)	Dose of dye (g/L)	Adsroption time (min)	Optimal pH	H(%) – q_{max} (mg/g)	Ref.
Powdered tourmaline	DR23	4.10^{-5} mol/L	4.0	180	3	153	[47]
Sepiolite	RB15	20	2.0	180	6	31.98	[50]
Cassava root husk	Direct Black ECO TFA	100	6.0	24 × 60	2	46.1	[43]
Nano round polycrystalline	Congo Red (CR)	200	1.6	100	2	77.4%; 98,216	[51]
NBRC 1658 strain	RY18	300	10	24 × 60	2	88% – 90.17	[52]
	AR18		10		2	56% – 129.53	
	BB41		10		9	75% – 729.92	
Clay	Astrazon Red	100	2.0	60	—	95% – 67.11	[53]
	Astrazon Blue	125	1.5	60	—	90% – 90.91	
Algerian kaolinite (DD3)	MB	75	1.0	60	Unadjus-ted pH (7)	44.48	[54]
EPGAC	DY12	125	3.0	120	2	42.01	[55]
FC3	DR79	50	0.8	120	3	79% – 44.07	This work

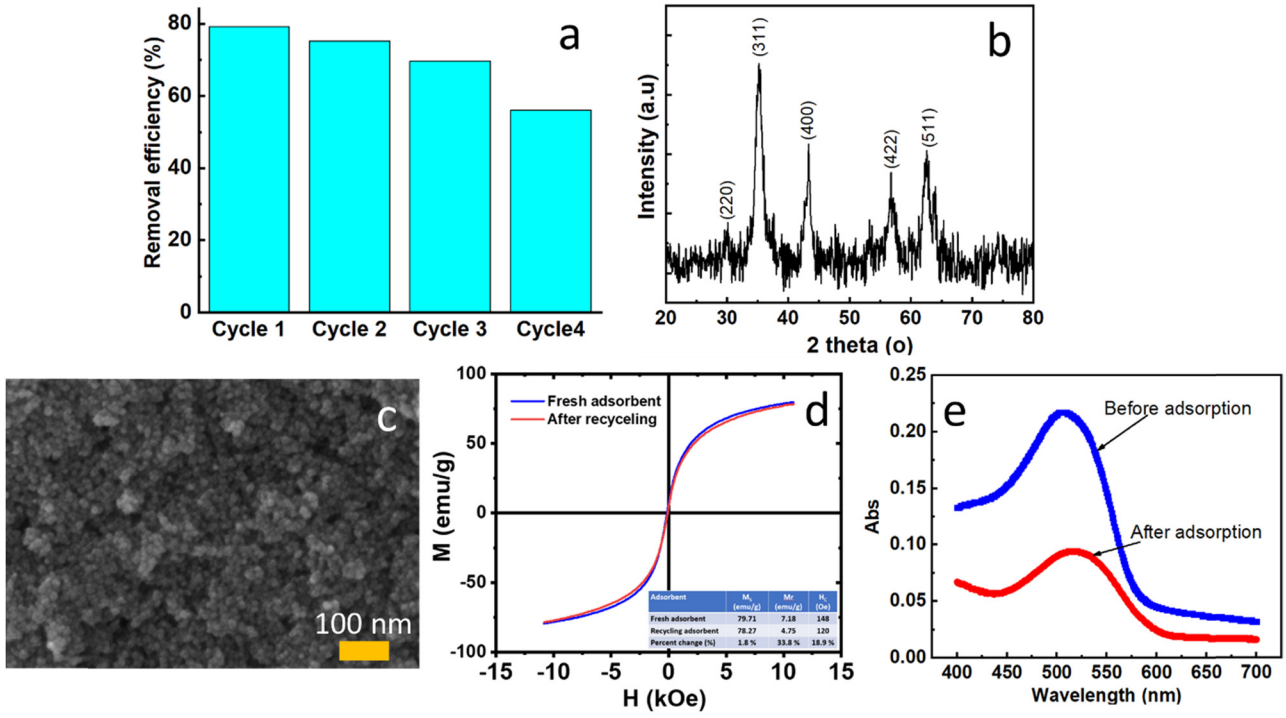

Figure 10: (a) Recycling of FC3 in the removal of DR79 (pH: 3, dose: 0.8 g/L, DR79 initial concentration: 50 mg/L), (b) XRD, (c) FESEM and (d) VSM analysis after four recovery steps, and (e) UV–Vis spectrum of the real wastewater sample before and after 120 min of adsorption (pH: 3, nano-adsorbent dosage: 0.8 g/L).

3.2.10 Chemical stability and reusability

From both economic and environmental perspectives, the recovery and reuse of adsorbent materials are crucial. Due to their strong magnetic properties, FC3 magnetic nanoparticles can be easily separated from the medium using a magnet. After the adsorbent was removed from the treatment medium, it was washed multiple times, first with double-distilled water and then with ethanol, until the washing solution was free of DR79 color [57]. The adsorbent was then dried in an oven at 80°C for 24 h before being subjected to reuse evaluation. Four regeneration cycles were conducted to assess the performance of the reused adsorbent. The DR79 removal efficiency of FC3 magnetic nanoparticles decreased from 79% in the first cycle to 67%. After four regeneration cycles, the efficiency dropped to 42% (DR79: 50 mg/L; 0.8 g/L; pH 3) under the same conditions Figure 10(a). This decline in efficiency may be attributed to the occupation of active sites on the adsorbent surface by DR79 molecules during previous adsorption cycles. According to Nasiri et al., the $ZnCoFe_2O_4$@Ch magnetic nano-adsorbent demonstrated an adsorption efficiency of 65% after five cycles of reuse for Tetracycline removal [58]. The structure of the material after the adsorption cycles was examined using XRD, FESEM, and VSM, as shown in Figure 10(b–d), indicating that the spinel ferrite structure of the FC3 material remained intact after four adsorption cycles. Additionally, the chemical stability of $Co_xFe_{1-x}Fe_2O_4$ was evaluated by determining the concentrations of Co and Fe in the solution using atomic absorption spectroscopy with the spectrophotometer (ASS NOVAA 400p) at wavelengths of 241.7 and 243.3 nm, respectively. According to the measurements obtained from the equipment, the concentration of Co is 0.99 mg/L, which meets the permissible limit for Co (1.0 mg/L) in irrigation water [59]. Meanwhile, the concentration of Fe is 2.15 mg/L, which complies with the WHO standard for Fe content in industrial wastewater, where the permissible limit is 5 mg/L.

4 Conclusion

Ferromagnetic nanoparticles $Co_xFe_{1-x}Fe_2O_4$ (x = 0–1) with spinel structural were synthesized via co-precipitation in which the formation of extremely small magnetic nanoparticles owing to sudden nucleation at elevated temperatures. These nanosized particles contributed to increased specific surface area of the material, thereby enhancing its adsorption capacity. Importantly, the ferromagnetic

properties of $Co_xFe_{1-x}Fe_2O_4$ exhibited superior environmental stability to Fe_3O_4 oxide. The adsorption performance of $Co_xFe_{1-x}Fe_2O_4$ toward DR79, particularly noteworthy for its effectiveness at low pH, demonstrated its potential as a highly efficient adsorbent. Moreover, the magnetic properties of the material facilitated easy recovery post-adsorption. The optimal adsorption occurred at $x = 0.5$. Adsorption behavior was systematically analyzed using the Langmuir, Freundlich, Temkin, and Redlich–Peterson models. The Langmuir and Redlich–Peterson models proved to be the most suitable. Among the investigated kinetic models, pseudo-second-order kinetics was determined to be the most appropriate. This study provides valuable insights into the synthesis, characterization, and application of $Co_xFe_{1-x}Fe_2O_4$ materials for the efficient removal of DR79. After four cycles of recovery and reuse, the material demonstrated a strong color removal efficiency while maintaining commendable chemical stability. Specifically, the material achieved an adsorption efficiency of 57% for color removal and 54.5% for COD reduction in an actual textile wastewater sample, promising its potential for future environmental remediation applications.

Funding information: This work was financially supported by Thai Nguyen University of Education under project number TNUE-2023-04.

Author contributions: Vu Thi Hau: writing – original draft; Pham Hoai Linh: formal analysis; Pham Thu Ha: data curation; Nguyen Thuy Chinh: methodology; Ngo Thi Mai Viet: methodology; Dang Duc Dung: formal analysis; Nguyen Quoc Dung: writing – review & editing; Thi Kim Ngan Tran: resources, validation.

Conflict of interest: The authors declare that they have no conflict of interest.

Ethical approval: The conducted research is not related to either human or animal use.

Data availability statement: All data generated or analyzed during this study are included in this published article.

References

[1] Kandisa RV, Saibaba KN, Shaik KB, Gopinath R. Dye removal by adsorption: a review. J Biorem Biodegrad. 2016;7(6):371.

[2] Ziane S, Bessaha F, Marouf-Khelifa K, Khelifa A. Single and binary adsorption of reactive black 5 and Congo red on modified dolomite: Performance and mechanism. J Mol Liq. 2018;249:1245–53.

[3] Fard MHA, Nasiri A, Daraei H. Green synthesis of AgCoFe. sub. 2O. sub. 4@ Ch/AC as a recyclable, magnetic nanohybrid heterogeneous catalyst in photodegradation of ceftriaxone from aqueous solutions with effluent bioassay. Appl Water Sci. 2023;13(11):NA-NA.

[4] Gharaghani MA, Samaei M, Mahdizadeh H, Nasiri A, Keshtkar M, Mohammadpour A, et al. An effective magnetic nanobiocomposite: Preparation, characterization and its application for adsorption removal of P-nitroaniline from aquatic environments. Environ Res. 2024;246:118128.

[5] Rafiq A, Ikram M, Ali S, Niaz F, Khan M, Khan Q, et al. Photocatalytic degradation of dyes using semiconductor photocatalysts to clean industrial water pollution. J Ind Eng Chem. 2021;97:111–28.

[6] Sarkodie B, Amesimeku J, Frimpong C, Howard EK, Feng Q, Xu Z. Photocatalytic degradation of dyes by novel electrospun nanofibers: A review. Chemosphere. 2023;313:137654.

[7] Arif N, Ma Y, Zafar MN, Humayun M, Bououdina M, Zhang SY, et al. Design and fabrication of biomass derived black carbon modified g-C_3N_4/$FeIn_2S_4$ heterojunction as highly efficient photocatalyst for wastewater treatment. Small. 2024;20(20):2308908.

[8] Gan Y, Ding C, Xu B, Liu Z, Zhang S, Cui Y, et al. Antimony (Sb) pollution control by coagulation and membrane filtration in water/wastewater treatment: A comprehensive review. J Hazard Mater. 2023;442:130072.

[9] Chen L, Xue Y, Luo T, Wu F, Alshawabkeh AN. Electrolysis-assisted UV/sulfite oxidation for water treatment with automatic adjustments of solution pH and dissolved oxygen. Chem Eng J. 2021;403:126278.

[10] Zhang H, Quan H, Yin S, Sun L, Lu H. Unraveling the toxicity associated with ciprofloxacin biodegradation in biological wastewater treatment. Environ Sci Technol. 2022;56(22):15941–52.

[11] Pohl A. Removal of heavy metal ions from water and wastewaters by sulfur-containing precipitation agents. Water, Air, Soil Pollut. 2020;231(10):503.

[12] Li Z, Huang Y, Wang X, Wang D, Wang X, Han F. Three-dimensional hierarchical structures of ZnO nanorods as a structure adsorbent for water treatment. J Mater Sci Technol. 2017;33(8):864–8.

[13] Elbasuney S, Elsayed MA, Mostafa SF, Khalil WF. MnO_2 nanoparticles supported on porous Al_2O_3 substrate for wastewater treatment: Synergy of adsorption, oxidation, and photocatalysis. J Inorg Organomet Polym Mater. 2019;29:827–40.

[14] Paswan SK, Kumar P, Singh RK, Shukla SK, Kumar L. Spinel ferrite magnetic nanoparticles: an alternative for wastewater treatment. In: Pollutants and water management: Resources, strategies and scarcity. John Wiley & Sons Ltd.; 2021. p. 273–305.

[15] Reddy DHK, Yun YS. Spinel ferrite magnetic adsorbents: alternative future materials for water purification? Coord Chem Rev. 2016;315:90–111.

[16] Rashid R, Shafiq I, Akhter P, Iqbal MJ, Hussain M. A state-of-the-art review on wastewater treatment techniques: the effectiveness of adsorption method. Environ Sci Pollut Res. 2021;28:9050–66.

[17] Li X-M, Xu G, Liu Y, He T. Magnetic Fe_3O_4 nanoparticles: Synthesis and application in water treatment. Nanosci Nanotechnology-Asia. 2011;1(1):14–24.

[18] Zeng H, Qiao T, Zhai L, Zhang J, Li D. Fe_3O_4@C particles synthesized with iron-containing water treatment residuals and its potential for methylene blue removal. J Chem Technol Biotechnol. 2019;94(12):3970–80.

[19] Kefeni KK, Mamba BB, Msagati TA. Application of spinel ferrite nanoparticles in water and wastewater treatment: a review. Sep Purif Technol. 2017;188:399–422.
[20] Konicki W, Sibera D, Mijowska E, Lendzion-Bieluń Z, Narkiewicz U. Equilibrium and kinetic studies on acid dye Acid Red 88 adsorption by magnetic $ZnFe_2O_4$ spinel ferrite nanoparticles. J Colloid Interface Sci. 2013;398:152–60.
[21] Khosravi I, Eftekhar M. Characterization and evaluation catalytic efficiency of $NiFe_2O_4$ nano spinel in removal of reactive dye from aqueous solution. Powder Technol. 2013;250:147–53.
[22] Nithya R, Thirunavukkarasu A, Sathya AB, Sivashankar R. Magnetic materials and magnetic separation of dyes from aqueous solutions: a review. Environ Chem Lett. 2021;19:1275–94.
[23] Muliwa AM, Leswifi TY, Onyango MS, Maity A. Magnetic adsorption separation (MAS) process: An alternative method of extracting Cr (VI) from aqueous solution using polypyrrole coated Fe_3O_4 nanocomposites. Sep Purif Technol. 2016;158:250–8.
[24] Chi Z, Zhu Y, Liu W, Huang H, Li H. Selective removal of As(III) using magnetic graphene oxide ion-imprinted polymer in porous media: Potential effect of external magnetic field. J Environ Chem Eng. 2021;9(4):105671.
[25] Pormazar SM, Dalvand A. Adsorption of Direct Red 23 dye from aqueous solution by means of modified montmorillonite nanoclay as a superadsorbent: mechanism, kinetic and isotherm studies. Korean J Chem Eng. 2020;37:2192–201.
[26] Kavcı E. Adsorption of Direct Red 243 dye onto clay: Kinetic study and isotherm analysis. Desalin Water Treat. 2021;212:452–61.
[27] Chavarriaga E, Lopera A, Franco V, Bergmann C, Alarcón J. Gel combustion synthesis and magnetic properties of $CoFe_2O_4$, $ZnFe_2O_4$, and $MgFe_2O_4$ using 6-aminohexanoic acid as a new fuel. J Magn Magn Mater. 2020;497:166054.
[28] Hakeem A, Alshahrani T, Muhammad G, Alhossainy M, Laref A, Khan AR, et al. Magnetic, dielectric and structural properties of spinel ferrites synthesized by sol-gel method. J Mater Res Technol. 2021;11:158–69.
[29] Majid F, Rauf J, Ata S, Bibi I, Malik A, Ibrahim SM, et al. Synthesis and characterization of $NiFe_2O_4$ ferrite: Sol–gel and hydrothermal synthesis routes effect on magnetic, structural and dielectric characteristics. Mater Chem Phys. 2021;258:123888.
[30] Kurian J, Lahiri B, Mathew MJ, Philip J. High magnetic fluid hyperthermia efficiency in copper ferrite nanoparticles prepared by solvothermal and hydrothermal methods. J Magn Magn Mater. 2021;538:168233.
[31] Zhang X, Chen Z, Wu C, Zhang J, Wang F. Solvothermal synthesis of spinel $ZnFe_2O_4$ nanoparticles with enhanced infrared radiation property. Chem Phys Lett. 2019;732:136647.
[32] Andersen HL, Granados-Miralles C, Jensen KM, Saura-Múzquiz M, Christensen M. The chemistry of spinel ferrite nanoparticle nucleation, crystallization, and growth. ACS Nano. 2024;18(14):9852–70.
[33] Ayawei N, Ebelegi AN, Wankasi D. Modelling and interpretation of adsorption isotherms. J Chem. 2017;2017:3039817.
[34] Sangsuriyonk K, Paradee N, Rotjanasuworapong K, Sirivat A. Synthesis and characterization of $Co_xFe_{1-x}Fe_2O_4$ nanoparticles by anionic, cationic, and non-ionic surfactant templates via co-precipitation. Sci Rep. 2022;12(1):4611.
[35] Köseoğlu Y, Bay M, Tan M, Baykal A, Sözeri H, Topkaya R, et al. Magnetic and dielectric properties of $Mn_{0.2}Ni_{0.8}Fe_2O_4$ nanoparticles synthesized by PEG-assisted hydrothermal method. J Nanopart Res. 2011;13:2235–44.
[36] Gonzalez-Sandoval M, Beesley A, Miki-Yoshida M, Fuentes-Cobas L, Matutes-Aquino J. Comparative study of the microstructural and magnetic properties of spinel ferrites obtained by co-precipitation. J Alloy Compd. 2004;369(1–2):190–4.
[37] Sharifi I, Shokrollahi H, Doroodmand MM, Safi R. Magnetic and structural studies on $CoFe_2O_4$ nanoparticles synthesized by co-precipitation, normal micelles and reverse micelles methods. J Magn Magn Mater. 2012;324(10):1854–61.
[38] Houshiar M, Zebhi F, Razi ZJ, Alidoust A, Askari Z. Synthesis of cobalt ferrite ($CoFe_2O_4$) nanoparticles using combustion, coprecipitation, and precipitation methods: A comparison study of size, structural, and magnetic properties. J Magn Magn Mater. 2014;371:43–8.
[39] Sathya A, Guardia P, Brescia R, Silvestri N, Pugliese G, Nitti S, et al. $Co_xFe_{3-x}O_4$ nanocubes for theranostic applications: effect of cobalt content and particle size. Chem Mater. 2016;28(6):1769–80.
[40] Biswal D, Peeples BN, Peeples C, Pradhan AK. Tuning of magnetic properties in cobalt ferrite by varying Fe^{+2} and Co^{+2} molar ratios. J Magn Magn Mater. 2013;345:1–6.
[41] Wong S, Tumari HH, Ngadi N, Mohamed NB, Hassan O, Mat R, et al. Adsorption of anionic dyes on spent tea leaves modified with polyethyleneimine (PEI-STL). J Clean Prod. 2019;206:394–406.
[42] Durairaj K, Senthilkumar P, Velmurugan P, Divyabharathi S, Kavitha D. Development of activated carbon from Nerium oleander flower and their rapid adsorption of direct and reactive dyes. Int J Green Energy. 2019;16(7):573–82.
[43] Scheufele FB, Staudt J, Ueda MH, Ribeiro C, Steffen V, Borba CE, et al. Biosorption of direct black dye by cassava root husks: Kinetics, equilibrium, thermodynamics and mechanism assessment. J Environ Chem Eng. 2020;8(2):103533.
[44] Safa Y, Bhatti HN. Kinetic and thermodynamic modeling for the removal of Direct Red-31 and Direct Orange-26 dyes from aqueous solutions by rice husk. Desalination. 2011;272(1–3):313–22.
[45] Mahmoodi NM, Arami M, Bahrami H, Khorramfar S. The effect of pH on the removal of anionic dyes from colored textile wastewater using a biosorbent. J Appl Polym Sci. 2011;120(5):2996–3003.
[46] AG ES, AM G, Mansour HF. Potential application of orange peel as an eco-friendly adsorbent for textile dyeing effluents. Res J Text Appar. 2013;17(4):31–9.
[47] Liu N, Wang H, Weng CH, Hwang CC. Adsorption characteristics of Direct Red 23 azo dye onto powdered tourmaline. Arab J Chem. 2018;11(8):1281–91.
[48] Liu J, Wang N, Zhang H, Baeyens J. Adsorption of Congo red dye on $Fe_xCo_{3-x}O_4$ nanoparticles. J Environ Manag. 2019;238:473–83.
[49] Kale RD, Potdar T, Gorade V. Treatment of CI Reactive Blue-21 effluent by microcrystalline cellulose grafted with APTES: kinetics, isotherm and thermodynamic study. Sustain Environ Res. 2019;29:1–12.
[50] Tabak A, Eren E, Afsin B, Caglar B. Determination of adsorptive properties of a Turkish Sepiolite for removal of Reactive Blue 15 anionic dye from aqueous solutions. J Hazard Mater. 2009;161(2–3):1087–94.
[51] Ofudje EA, Al-Ahmary KM, Alshdoukhi IF, Alrahili MR, Kavil YN, Alelyani SS, et al. Nano round polycrystalline adsorbent of chicken bones origin for Congo red dye adsorption. Sci Rep. 2024;14(1):7809.
[52] Hassan Ibrahim AH, Cihangir N, Idil N, Aracagök YD. Adsorption of azo dye by biomass and immobilized Yarrowia lipolytica;

equilibrium, kinetic and thermodynamic studies. World J Microbiol Biotechnol. 2024;40(5):140.

[53] Açıkyıldız M, Gürses A, Güneş K, Şahin E. Adsorption of textile dyes from aqueous solutions onto clay: Kinetic modelling and equilibrium isotherm analysis. Front Chem. 2023;11:1156457.

[54] Hamri N, Imessaoudene A, Hadadi A, Cheikh S, Boukerroui A, Bollinger J-C, et al. Enhanced adsorption capacity of methylene blue dye onto kaolin through acid treatment: batch adsorption and machine learning studies. Water. 2024;16(2):243.

[55] Reddy YS, Jose TJ, Dinesh B, Kumar RN, Kumar PS, Kaviyarasu K. Equilibrium, kinetic, and thermodynamic study of Direct Yellow 12 dye adsorption by biomass-derived porous graphitic activated carbon. Biomass Convers Biorefin. 2024;1–17.

[56] Mehrabanpour N, Nezamzadeh-Ejhieh A, Ghattavi S. A comparative photocatalytic activity between PbS NPs and PbS-clinoptilolite towards Cefotaxime. Solid State Sci. 2022;131:106953.

[57] Rajabi S, Derakhshan Z, Nasiri A, Feilizadeh M, Mohammadpour A, Salmani M, et al. Synergistic degradation of metronidazole and penicillin G in aqueous solutions using $AgZnFe_2O_4$@ chitosan nanophotocatalyst under UV/persulfate activation. Environ Technol Innov. 2024;35:103724.

[58] Nasiri A, Golestani N, Rajabi S, Hashemi M. Facile and green synthesis of recyclable, environmentally friendly, chemically stable, and cost-effective magnetic nanohybrid adsorbent for tetracycline adsorption. Heliyon. 2024;10(2):1–21.

[59] Mahmud HN, Huq AO, binti Yahya R. The removal of heavy metal ions from wastewater/aqueous solution using polypyrrole-based adsorbents: a review. Rsc Adv. 2016;6(18):14778–91.